Analysis of swirling flow in hydrocyclones operating under dense regime

Aurélien Davailles, Éric Climent, Florent Bourgeois, Arun Kumar Majumder

Analysis of swirling flow in hydrocyclones operating under dense regime

Aurélien Davailles [a,b], Eric Climent [a,b,*], Florent Bourgeois [b,c], Arun Kumar Majumder [d]

[a] Université de Toulouse, INPT, UPS, IMFT (Institut de Mécanique des Fluides de Toulouse), Allée Camille Soula, F-31400 Toulouse, France
[b] CNRS, Fédération de recherche FERMAT, Toulouse, France
[c] Université de Toulouse, INPT, UPS, LGC (Laboratoire de Génie Chimique), 4 Allée Emile Monso, BP 44362, 31432 Toulouse Cedex 4, France
[d] Department of Mining Engineering, Indian Institute of Technology, Kharagpur 721 302, India

A B S T R A C T

There are many circumstances where hydrocyclone performance and dense flow are intertwined, such as for example when feed solids flow exceeds hydrocyclone capacity during continuous operations. The work reported here, which is part of an ongoing research effort to develop a robust CFD model for prediction of hydrocyclone performance, focuses on hydrocyclone operation under high solids concentration. The paper presents the basic physics framework that accounts for solid–liquid and solid–solid interactions under hydrocyclone's swirling flow. Operating conditions that are past the transition from spray to rope regime are deliberately chosen for this purpose. Model predictions are validated by comparison with solids split and separation curves measured on a 100 mm diameter hydrocyclone. CFD model predictions permit taking an insightful look at the inside of a hydrocyclone under extreme operating conditions, which would be difficult to achieve experimentally. Velocity profiles, G-force distribution and distribution of solids predicted by CFD are bound to lead to a better understanding of the separation that takes place inside a hydrocyclone, which may eventually help improve hydrocyclone design and performance.

1. Introduction

There are many circumstances where hydrocyclone performance and dense flow are intertwined, such as for example when feed solids flow exceeds hydrocyclone capacity during continuous operations. Moreover, under normal operating conditions, it is generally perceived that some regions inside a hydrocyclone might be very densely populated with solids while other regions might only experience dilute conditions. Dilute conditions are expected in the central part of the hydrocyclone and in the cylindrical section of the hydrocyclone, whereas dense conditions, as dense as packed beds in some instances, can be expected along the hydrocyclone walls as well as in the conical region. With the above in mind, solid–solid separation inside a hydrocyclone is bound to vary significantly throughout the body of an operating hydrocyclone. This reasoning emphasizes the need to better understand particle and water flow behavior inside a hydrocyclone under high solids concentration, whether dense regions occur locally or spread throughout the hydrocyclone body. In an ongoing research effort, therefore, an attempt has been made to develop a robust CFD model for the prediction of hydrocyclone performances at different operating conditions. The physics of particle separation behavior inside a hydrocyclone at dilute conditions and the CFD simulation have already been described elsewhere (Davailles et al., in press). The present article, however, deals with the CFD modeling of a hydrocyclone at high solids concentrations.

1.1. Experimental studies

The hydrodynamic behavior of a hydrocyclone depends on inlet solid concentration, feed flow rate and geometry of the device. Fig. 1 presents two distinct behaviors, below and above the transition to roping (Neesse et al., 2004a). Under those two operating regimes, visualization of solid–liquid flow patterns is difficult as the accumulation of particles along the wall highly complicates the optical access to the hydrocyclone's core. Usual techniques which have been applied to study single phase flow, such as Laser Doppler Velocimetry (Hsieh, 1988), are not applicable for concentrated systems. Much more complex measurement tools, such as X-ray tomography (Galvin and Smitham, 1994) or radioactive particle tracking (Chang et al., 2011), have, therefore, been tried. However, it is still very challenging to gain new experimental insights into local hydrodynamics of dense solid–liquid flows. At low feed solids concentration, the underflow discharge of a hydrocyclone has a spray profile and a stable air core is established due to the suction of air through the underflow (Fig. 1a). However, with increasing feed solids concentration the quantity of solids exiting through

* Corresponding author at: Université de Toulouse, INPT, UPS, IMFT (Institut de Mécanique des Fluides de Toulouse), Allée Camille Soula, F-31400 Toulouse, France.
E-mail addresses: aurelien.davailles@imft.fr (A. Davailles), eric.climent@imft.fr (E. Climent), florent.bourgeois@ensiacet.fr (F. Bourgeois), majumder1965@gmail.com (A.K. Majumder).

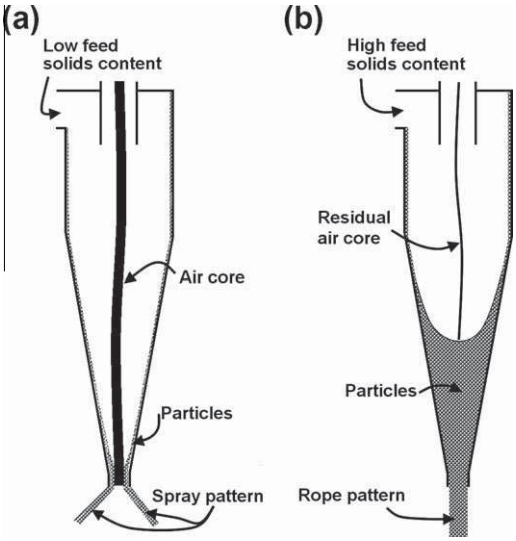

Fig. 1. Hydrocyclone: (a) dilute and (b) dense slurries.

the underflow discharge also increases and above a critical point (Neesse et al., 2004b) the rate of accumulation of solids in the conical portion exceeds the rate of discharge. As a result the spray profile collapses and the air suction is also hindered. This condition is generally termed as roping (Fig. 1b). Neesse and Dueck (2007) opined that the air core cannot totally disappear while the exit is plugged by particles. An air core remains within the hydrocyclone and vanishes on the particles bed. However, the small size of the air core and the absence of connection with the atmosphere severely limit its influence on the hydrodynamics for this operating regime.

1.2. Numerical simulations and the objectives

CFD studies on hydrocyclones generally aim at giving new insights on local flow patterns, such as velocity profiles, pressure distribution and spatial distribution of solids. These information are difficult to access through experimentation and are critical for better understanding of separation performances.

However, numerical modeling of all physical aspects still remains a challenging research topic due to the complexities associated with the swirling flow behavior of concentrated slurries within a hydrocyclone. The geometry is not an obvious one and contributes significantly to flow streams repartition between the two exits. The level of turbulence is high corresponding to a hierarchy of spatial flow structures interacting selectively with the particles. Due to strong swirling, the anisotropy of the flow couples particle centrifugation and triggers air focusing in the core of the device. The intrinsic three phase (gas–liquid–solid) flow with a large amount of particles make hydrocyclones a real challenge for CFD codes.

Large Eddy Simulation (LES) appears to be the most promising approach for modeling flow turbulence under dilute feed flow rate (Slack et al., 2000; Delgadillo and Rajamani, 2005) as it preserves turbulence spatial structure. For particle laden flows, LES can be coupled with Discrete Particle Simulation. Without momentum coupling between the solid phase and the liquid phase, this permits to evaluate separation curves under dilute regime based on trajectory analysis. Unfortunately, this technique is very time consuming and the relevance of the model for concentrated slurries needs further theoretical developments and validation tests on academic configurations. This approach is still reserved for small scale study and only thousands of particles, while the work that is presented here is concerned with the simulation of industrial size hydrocyclones and dense suspensions. This implies a degree of compromise between the accuracy of the physics and the computational cost.

Processes at both the macroscopic and local scales have some influences on hydrocyclone's behavior; hence both scales must be embedded in models for making prediction of hydrocyclone performance. Quite a few experimental and numerical studies helped build a strong understanding of single-phase flow inside hydrocyclones (Kelsall, 1952; Hsieh and Rajamani, 1991; Brennan, 2006).

In contrast, the sensitivity of separation performance to feed solids concentration possibly has not been studied so far and, therefore, remains unexplained. One reason for this situation is that the measurement of slurry velocity profiles or solids spatial distribution anywhere inside the hydrocyclone is an experimentally challenging task.

It is comparatively simple to obtain such information from CFD simulations based on the understanding of swirling flow patterns inside a hydrocyclone. The physics and the CFD modeling dealing with dilute suspensions was validated with our experimental data as well as with a set of published data (Davailles et al., in press). The present study focuses on the analysis of swirling flow in hydrocyclones operating under dense flow regimes having the following objectives:

- Development of a modeling scheme based on the strong foundation of physics of fluid flow and particle–fluid interactions.
- Simulation of the roping conditions in a 100 mm diameter hydrocyclone using an Eulerian multi fluid model with RANS turbulence modeling.
- Validation of the model predicted data with experimental data.

It is not within the scope of this paper to investigate the transition between spray and rope discharge despite the occurrence of this transition is an important issue from an operational standpoint. Indeed, the issue at stake here is that of the effect of dense suspension on swirling patterns and particle separation inside the hydrocyclone. This yields the choice of operating conditions used throughout this work.

2. Description of CFD model

The three dimensional numerical simulations were performed with NEPTUNE_CFD v1.08@Tlse (Laviéville and Simonin, 1999, 2006; Ozel et al., 2010; Galassi et al., 2009). NEPTUNE_CFD is a multiphase flow simulation software developed within the framework of a French industrial consortium.

The behavior of dispersed multiphase flow is modeled using the general Eulerian multi-fields balance equations which are obtained from the fundamental conservation laws of physics (mass conservation and momentum balance), restricted to Newtonian mechanics. Conservation laws are written under differential form that are valid at any time and location within the continuum, except across interfaces between two physical phases. At interfaces, jump conditions derived from continuous equations are written and integrated through source and sink terms in the equations. This results in a fully coupled set of equations.

2.1. Transport equations

The multiphase Eulerian model is built on a kinetic approach based on a joint fluid-particle Probability Density Function (Simonin, 1996). The set of PDF's moment transport equations (mass, momentum, particle agitation) is derived from a Boltzmann-like kinetic equation of the PDF.

The multi-field mass balance equation for field k is written (when $k = l$, we refer to the liquid and $k = p$ to the class p of particles):

$$\frac{\partial}{\partial t}(\alpha_k \rho_k) + \frac{\partial}{\partial x_i}(\alpha_k \rho_k U_{k,i}) = 0 \tag{1}$$

with α_k, ρ_k, U_k, the volumetric fraction, the density and the mean velocity of phase k.

The multi-fluid momentum balance equation for phase k is defined as follows:

$$\frac{\partial}{\partial t}(\alpha_k \rho_k U_{k,i}) + \frac{\partial}{\partial x_j}(\alpha_k \rho_k U_{k,j} U_{k,i}) = -\alpha_k \frac{\partial P}{\partial x_i} + \sum_{q=p,g} I_{(q\to k),i} + \alpha_k \rho_k g_i + \frac{\partial}{\partial x_j} T_{k,ij} \tag{2}$$

with P the mean pressure, g_i the acceleration due to gravity and $T_{k,ij}$ the effective stress tensor.

$I_{(l\to p),i}$ accounts for momentum transfer rate from the liquid to solid phase (friction), while $I_{(q\to p),i}$ represents the momentum exchange by collision between particles q and p. In order to account for collisions between different particle sizes, the mean momentum transfer between phases $I_{(q\to p),i}$ has been generalized in this study compared to the validation on dilute regime (Davailles et al. (in press)).

The mean liquid to particle momentum transfer can be modeled using an estimate of the drag acting on particles.

$$I_{(l\to p),i} = -I_{(p\to l),i} = \frac{\alpha_p \rho_p}{\tau_{lp}^F} V_{r,i} \tag{3}$$

$$\text{with } \frac{1}{\tau_{lp}^F} = \frac{3}{4}\frac{\rho_l \langle C_D \rangle_p}{\rho_p d_p} \langle |V_r| \rangle \tag{4}$$

τ_{lp}^F is the particle relaxation time scale, and $\langle\ \rangle_p$ is the ensemble average operator over the particulate phase (Simonin, 1996). $V_{r,i}$ is the average of the local relative velocity which can be expressed in terms of the averaged velocity between phases and the drift velocity. The mean drag coefficient related to an isolated particle, $\langle C_D \rangle_p$ can be written as a function of particulate Reynolds number. Under moderately concentrated suspension to dense regime, the multi-fluid approach accounts for local particle volume fraction α_p through a correction to the drag law. Under these conditions, we adopt the approach published by Gobin et al. (2003), who proposed to use a combination of two relations: Wen and Yu (1965) for dilute cases and Ergun (1952) for concentrated regime.

$$\langle C_D \rangle_p = \begin{cases} \text{if} \quad \alpha_p > 0.3 \\ \quad \text{Min}\left[\left\langle C_D^{\text{Wen Yu}} \right\rangle_p ; \quad \left\langle C_D^{\text{Ergun}} \right\rangle_p \right] \\ \text{if} \quad \alpha_p \leqslant 0.3 \\ \quad \left\langle C_D^{\text{Wen Yu}} \right\rangle_p \end{cases} \tag{5}$$

with

$$\left\langle C_D^{\text{Ergun}} \right\rangle_p = 200\frac{\alpha_p}{\text{Re}_p} + \frac{7}{3} \tag{6}$$

$$\left\langle C_D^{\text{Wen Yu}} \right\rangle_p = \begin{cases} \text{if} \quad \text{Re}_p < 1000 \\ \quad \alpha_l^{-1.7}\frac{24}{\text{Re}_p}\left(1 + 0.15\text{Re}_p^{0.687}\right) \\ \text{if} \quad \text{Re}_p \geqslant 1000 \\ \quad 0.44\alpha_l^{-1.7} \end{cases} \tag{7}$$

$$\text{Re}_p = \frac{\alpha_l \rho_l d_p \langle |V_r| \rangle}{\mu_l} \tag{8}$$

According to Gourdel et al. (1999), the momentum exchange due to collisions between particle q and particle p can be written as:

$$I_{q\to p,i} = -\alpha_p \rho_p \frac{m_q}{m_p + m_q}\frac{1 + e_c}{2}\frac{H_1(Z_{pq})}{\tau_{pq}^c}(U_{p,i} - U_{q,i}) \tag{9}$$

m_p and m_q are respectively the mass of particle p and particle q, e_c is the inelastic restitution coefficient and τ_{pq}^c the collision characteristic time.

The momentum exchange term presented in Eq. (9) complements the monodisperse model. When $m_p = m_q$(monodisperse), $U_p = U_q$ yielding $I_{q\to p,i}$ equals to zero.

$H_1(Z_{pq})$ is a theoretical function that permits adapting the kinetic theory of gases to that of granular flow.

2.2. Turbulence modeling

Ensemble averaging is usually applied to instantaneous Navier–Stokes equations in order to study industrial flows. These new equations are called Reynolds Averaged Navier–Stokes (RANS) equations.

The effective stress tensor, $T_{k,ij}$, in Eq. (2) can be written as follows:

$$T_{k,ij} = \alpha_k \rho_k R_{k,ij} + \Theta_{k,ij} \tag{10}$$

It contains two contributions: a turbulent kinetic stress tensor $R_{k,ij}$ due to turbulence (or fluctuations in phase k) and a collisional (or molecular viscosity) term $\Theta_{k,ij}$for the solid (alt. liquid) phase. The constitutive relations for viscosity and diffusivity are derived in the framework of the kinetic theory for dry granular flows.

According to Batrak et al. (2005), the solid stress tensor $T_{p,ij}$ can be written as:

$$T_{p,ij} = \overbrace{\left[P_p - \lambda_p \frac{\partial U_{p,m}}{\partial x_m}\right]\delta_{ij}}^{\text{Kinetic stress}} - \underbrace{\mu_p\left[\frac{\partial U_{p,i}}{\partial x_j} + \frac{\partial U_{p,j}}{\partial x_i} - \frac{2}{3}\frac{\partial U_{p,m}}{\partial x_m}\delta_{ij}\right]}_{\text{Collisional stress}}$$

with $\mu_p = \mu_{p,col} + \mu_{p,cin} + \mu_{p,fric}$.

The terms $\mu_{p,col}$ and $\mu_{p,cin}$ represent the kinetic viscosity and the collisional viscosity respectively (Batrak et al. (2005)).

When the particulate volume concentration is high (typically $\alpha_p \geqslant 0.5$), the assumption of instantaneous binary collision is often inaccurate as enduring contacts are prone to occur. Frictional effects are accounted for by adding a frictional viscosity $\mu_{p,fric}$ as described by Srivastava and Sundaresan (2003).

Because of the strong anisotropy of the flow, the Reynolds Stress Model (RSM) due to Launder et al. (1975) seems naturally better suited than models based on an assumption of isotropy of the Reynolds stress tensor, such as the familiar $k-\epsilon$ turbulence model. With RSM, the turbulent viscosity approach has been complemented and the Reynolds stresses $\langle \rho_f u_{f,i} u_{f,j} \rangle_f$ are computed directly to close RANS equations. This is done by solving the differential transport equations, leading to heavier computational costs. The exact Reynolds stress transport equation accounts for the directional effects of the Reynolds stress fields. The Reynolds stress model has been extended to multiphase flows.

For the particles, particle fluctuating kinetic energy, q_p^2 and fluid-particle fluctuating velocity covariance, q_{fp} are solved through a set of coupled transport equations. For polydisperse solid phase, the particle agitation transport equation contains some specific terms (Gourdel et al., 1999; Batrak et al., 2005) that account for three phenomena: particle agitation dissipation by non-elastic polydisperse collisions, production of particle agitation by the mean solid relative velocity and finally, transfer of particle agitation between different classes of the solid phase.

2.3. Mesh and boundary conditions

The whole volume of the 100 mm diameter hydrocyclone has been meshed, as shown in Fig. 2. Simail software, which is associated to NEPTUNE_CFD v1.08@Tlse, was used to build the mesh. The 3D mesh was first generated by a full rotating extrusion of a cross-section of the hydrocyclone. Then, in order to prevent the existence of a singular axis at the center of the hydrocyclone, the cylindrical volume located around the central axis has been meshed separately. Overall, the total number of cells comprises 450,000 hexahedral and pentahedral structured control volumes.

Boundary conditions at the feed inlet are prescribed assuming a uniform distribution of solids across the section. Atmospheric pressure is imposed at the underflow and overflow exits. The suspension can leave the domain freely through those exits. Along the hydrocyclone walls, standard turbulent friction functions are used for the liquid phase (law of the wall). A zero flux condition is applied on the velocity field for particles $\left(\frac{dU_p}{dn} = 0\right)$.

3. Experimental work

As justified earlier, operating conditions were chosen past the transition from spray to rope, such that discharge of the 100 mm hydrocyclone pilot test rig was a steady rope.

3.1. Experimental set-up

The pilot test rig dimensions are reported in Fig. 3. Standard global information, including operating parameters and performance characteristics (partition function) can be accessed with this set-up.

The Neyrtec's HC100 hydrocyclone (100 mm diameter) is made of interchangeable polyurethane parts, allowing various geometrical configurations to be tested (see technical specifications in Table 1). The length of the cylindrical body can be adjusted using 100 mm extensions, and several diameter spigots (from 6 mm to 18 mm) are available. One 100 mm cylindrical extension was used for the experiments and simulations reported here, with either 6 mm or 18 mm diameter spigots. One single 50 mm vortex finder was use in the experiments.

The slurry is pumped around a closed circuit using a C40 SCHABAVER 2.2*kW* centrifugal pump. Both underflow and overflow are recirculated to a 1 m^3 agitated sump that feeds the hydrocyclone. Slurry mass flow rate is monitored using an FSM4000 electromagnetic flowmeter from ABB Automation Products GmbH. The mass flowmeter readings were calibrated from pure water flow up to 50 wt% solids (28 vol.%).

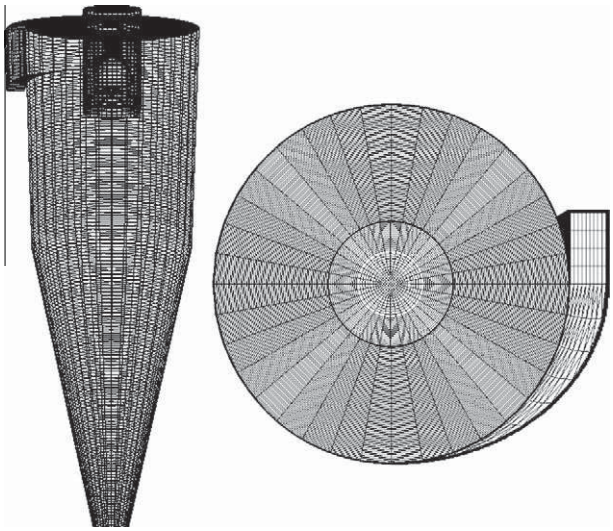

Fig. 2. Axial and cross-section view of the mesh.

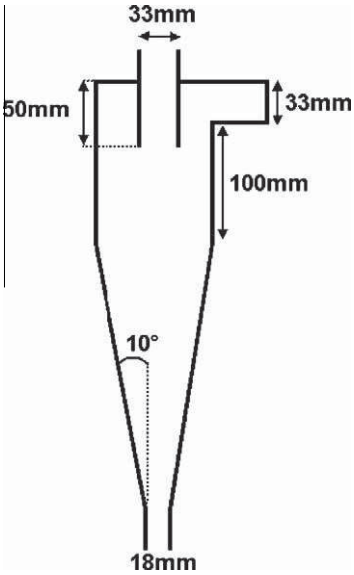

Fig. 3. Geometric features of Neyrtec's HC100 hydrocyclone.

Table 1
Nominal features of Neyrtec's HC100 hydrocyclone.

Model	HC 100
Diameter (mm)	100
Feed rate (m^3/h)	7–13.5
Feed pressure (kPa)	60–250
Cut size (μm)	7–18
Material	Polyurethane
Overflow (OF) diameter (mm)	33
Vortex finder length (mm)	50
Underflow (UF) diameter (mm)	18

Silica particles were used in the experiments. The particle size distribution is plotted in Fig. 4. The material itself is 98.8% SiO_2 (according to the manufacturer), hence it is assumed to consist of a single constituent with specific gravity 2.65.

It was found during the early phases of our work that the geometry of the simulated hydrocyclone should closely match the geometry of the real hydrocyclone, particularly in the inlet region. As seen in Fig. 5, the inlet pipe section is connected to the cylindrical body of the hydrocyclone through a rectangular and tangential channel through a 10 mm × 30 mm section. The sudden reduction in cross-sectional area forces a sharp increase of the inlet flow velocity, which the simulation must model accurately. Indeed, the initial velocity of water and particles as they enter the hydrocyclone are utterly critical.

3.2. Experimental results

This section presents the experimental data that were obtained with feed solids concentration in the range 10–50 wt% (4 vol.% and 27 vol.%).

3.2.1. Effect of feed solids concentration on hydrocyclone performance

The feed solids concentration was varied in 10 wt% increments between 10 wt% and 50 wt%. Feed volumetric flowrate was set to 2.6 10^{-3} m^3 s^{-1} (156 L min^{-1}). Overflow and underflow streams

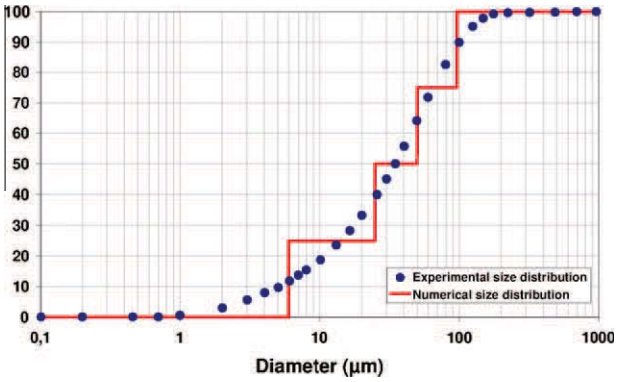

Fig. 4. Size distribution of silica particles: measured (symbols) and discretized for numerical simulation (solid line).

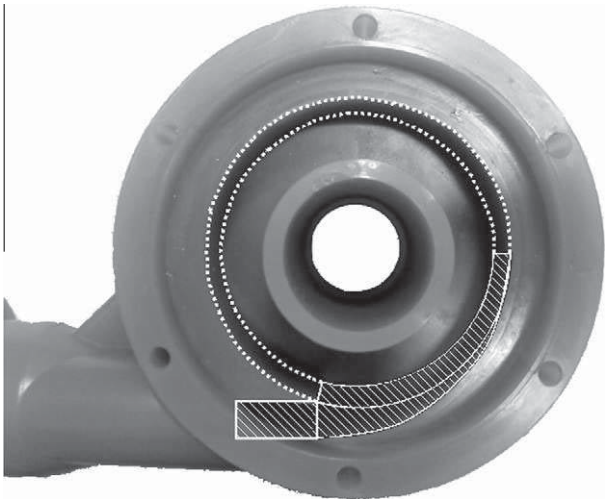

Fig. 5. HC100 injection.

were sampled manually by short successive cuts of the full streams. A sample of feed material was taken for every experiment at the hydrocyclone underflow, using a low flowrate for which all the slurry would report to the underflow. Particle size distributions of the feed, the underflow and the overflow were measured by laser diffractometry using a Malvern 2000S, using a silica refractive index of 1.49. Every data set was reconciled using standard mass balance techniques, from which partition curves were calculated.

Results obtained with the 18 mm diameter spigot are presented in Fig. 6 and reported in Table 2. The measurements follow expected trends for feed solids concentration and cut size, such as reported by Nageswararao et al. (2004). Indeed, the cut size (d_{50} or d_{50c}) and the concentration of solids in the underflow both increase with feed solids content. In addition, the steepness of the partition function slope (sharpness index SI) decreases as solids concentration is increased. Water recovery was not measured in this study. The values of water recovery to the underflow R_f, which are reported in Table 2 were read directly from the partition functions. These are found to increase from 2% to about 20% with feed solids concentration in the range 10–50 wt%. As expected, the performance of the hydrocyclone worsens monotonically with increasing feed solids concentration.

From 30 wt% solids concentration onwards, the underflow discharges as a rope. For sake of clarity, Fig. 7 shows the discharge of the hydrocyclone at 10 wt% (4 vol.%) and 30 wt% (14 vol.%) so the reader can readily appreciate the drastic change in flow pattern. It is noted that the hydrocyclone did not choke under the conditions of Table 2.

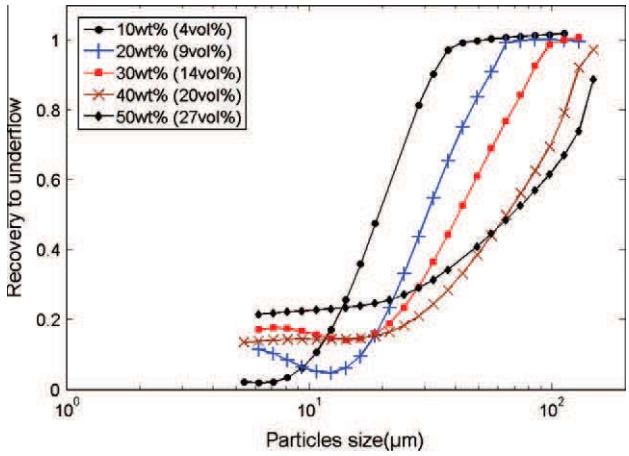

Fig. 6. Measured partition function for 10 wt% to 50 wt% feed solids concentration with the 18 mm diameter spigot.

Table 2
Feed solids concentration influence on cut-sizes and solids recovery to the underflow.

	d_{50} (μm)	d_{50c} (μm)	$\hat{\kappa}$	R_f (%)	SI
10 wt%	19.25	19.5	0.62	2.0	0.55
20 wt%	30.55	31.5	0.53	5.0	0.53
30 wt%	40.99	46.0	0.47	16.9	0.48
40 wt%	64.84	75.3	0.32	13.4	0.40
50 wt%	68.05	95.3	0.36	21.4	0.36

As the objective of this study is the understanding of the hydrocyclone hydrodynamics with roping discharge, this paper focuses on feed solids content higher than 30 wt% (14 vol.%).

3.2.2. Effect of spigot diameter

In order to provide different conditions against which to test CFD predictions, experiments were carried out using two spigot diameters, 6 mm and 18 mm. Clearly, reducing the spigot diameter with a roping hydrocyclone is a practical nonsense, however it makes sense in the context of creating additional dense regime conditions against which to test the CFD simulation model and study the swirling flow inside the hydrocyclone. Partition functions that were obtained with 30 wt% feed solids concentration are plotted in Fig. 8 for both spigot diameters. The important point here is that hydrocyclone performance changes significantly between these conditions, which reflect significant changes in water and particle flow inside the hydrocyclone. It is noted that some classification is still taking place despite the roping discharge of the hydrocyclone.

It was found that a threefold decrease in spigot diameter gave an increase in d_{50} from 37 μm to 91 μm under these roping conditions. Separation sharpness was similar with both spigots; however water recovery to underflow increased (from about 10% to 20%) with the larger spigot diameter.

4. Numerical simulation at high solids concentration

According to earlier statements from Section 2.3 about the absence of an air core at high solids concentration, which was also illustrated in Fig. 1, hydrocyclone operation in dense regime was computed by simulating water and solids phase only. The computational ease that is gained from having to simulate two phases

Fig. 7. Photographs of the underflow discharge with feed solid content of 10 wt% and 30 wt%.

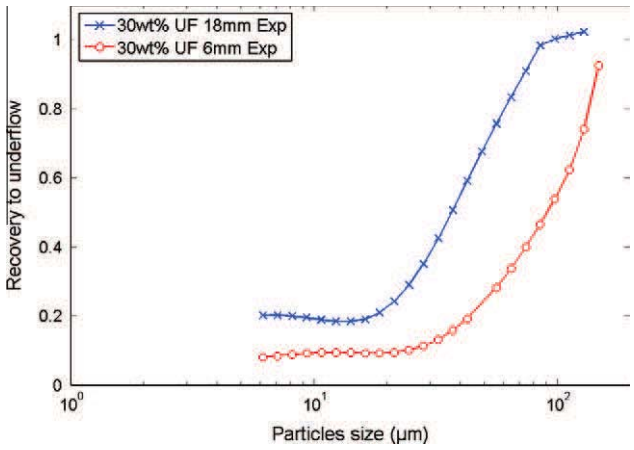

Fig. 8. Measured influence of spigot diameter on separation curves.

instead of three (with gas) is partly offset by the added complexity of simulating dense particle flow in the hydrocyclone.

The particle size distribution used in the experiments was discretized into four size classes, each class accounting for 25 wt% of the experimental size distribution. In the end, the simulation uses four types of particles with sizes equal to the arithmetic mean size of the four size classes. These four sizes are 6 μm, 25 μm, 50 μm and 96 μm respectively. Thus, the size distribution used in the simulations is a step function that follows the experimental size distribution. Both size distributions were plotted in Fig. 4.

The feed flowrate used in the simulation is set equal to the experimental flowrate (2.6 L s^{-1}). Water and silica mass flow rates, which depend on the solid to liquid ratio in the feed, are calculated using 1.0 s g. for water and 2.65 s g. for silica particles.

4.1. Effect of feed solids concentration

Partition functions predicted by numerical simulation, defined as the ratio of the mass flux of each particle size in the underflow to that in the feed, are presented in Fig. 9. Results obtained in very dilute condition (1 wt%) are used to illustrate the best separation that can be achieved with the hydrocyclone. With increasing feed solids content, separation efficiency is predicted to deteriorate as it is observed experimentally.

As with the measurements, the simulations predict that the recovery of water to underflow increases with feed solids concentration, with a significant increase between 40 wt% and 50 wt%.

These changes in hydrocyclone performance areassociated with a changing distribution of solids inside the hydrocyclone body. Table 3 gives the mass distribution of the water and the 4 size classes inside the hydrocyclone as a function of feed solids concentration. For consistency of the results, it can easily be verified from the data in Table 3 that the volume of water and solids inside the hydrocyclone is constant and equal to 1.82 L.

Results at 30 wt% and 40 wt% feed solids concentration are nearly same. Partition functions in Fig. 9 share the same shape and numerical results are close to each other. Table 3 shows a strong gradient between the mass of small and large particles inside the hydrocyclone, which reflects that a strong size classification effect is still taking place, despite the hydrocyclone operating in the roping regime. Solids concentration inside the hydrocyclone is also higher than the feed (36 wt% and 46 wt% against 30 wt% and 40 wt%), which indicates that the hydrocyclone is thickening the particles at the underflow. As it will be shown later, these results indicate that the hydrocyclone body length is such that even under roping conditions, there is sufficient body length inside which the flow is swirling for some classification to take place, giving particles sufficient residence time for separation to occur.

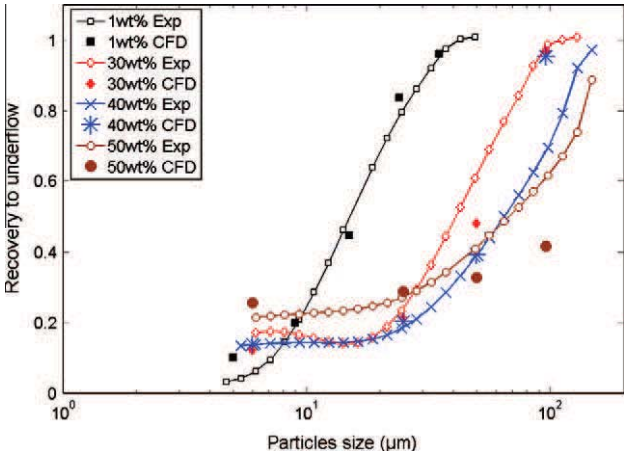

Fig. 9. CFD predictions of separation curve as a function of feed solids concentration (symbols: simulation, solid lines: experimental measurements).

Table 3
Mass distribution of water and solids inside the hydrocyclone body.

Inlet content	Water (kg)	Silica (kg)				
		6 μm	25 μm	50 μm	96 μm	Total
30 wt%	1.509	0.163	0.182	0.247	0.241	0.832
14 vol.%	64.4%	7.0%	7.8%	10.5%	10.3%	35.6%
40 wt%	1.376	0.231	0.249	0.322	0.383	1.185
20 vol.%	53.7%	9.0%	9.7%	12.6%	15.0%	46.3%
50 wt%	1.311	0.328	0.326	0.332	0.370	1.355
28 vol.%	49.2%	12.3%	12.2%	12.4%	13.9%	50.8%

As feed solids concentration is increased further, the gradient between the mass of small and large particles decreases, to the point where it is almost nil with the 50 wt% case. In this case, the solids distribution inside the hydrocyclone is almost equal to that of the feed. The solids concentration inside the hydrocyclone is 51%, which is also almost identical to the feed. There is hardly any classification taking place in this case, which indicates that there is hardly any zone inside the hydrocyclone where flow is swirling at a sufficiently high rate. This will be confirmed later through observation of solids concentration distribution inside the device.

The tangential velocity, which drives the separation inside the hydrocyclone, is strongly affected by the feed solid concentration. As shown in Fig. 10, tangential velocity predicted at 1 wt% is significantly higher than tangential velocity obtained at the high solids concentrations used in this study. Profiles at 30 wt% and 40 wt% are close to each other, which agrees with the closeness of the partition functions predicted at these concentrations (cf. Fig. 9). The same profile with 50 wt% solids content in the feed is very different, as was the partition function, with values of tangential velocity half those obtained at 30 wt% and 40 wt% solids concentrations.

Keeping in mind that the separation force is proportional to $\frac{U_{\theta p}^2}{rg}$ ($U_{\theta p}$ is the particles tangential velocity, r the radius and g the acceleration due to the gravity), the maximum value of this acceleration factor, which is a key separation driver decreases from about 900 for a feed solids content of 1 wt% to 280 for 30 wt%, 230 for 40 wt% and only 40 for 50 wt% (Fig. 11).

The reduction in tangential velocity is perhaps best understood when it is recognized that should the inside of the hydrocyclone rotate as a solid rotation, the tangential velocity would be linear. What this means is that increasing feed solids concentration yields velocity distribution in the hydrocyclone that tends to reduce the differential motion of particles, which then worsens particle separation. This change in behavior is entirely due to the concentration of solids inside the hydrocyclone, as shown hereafter.

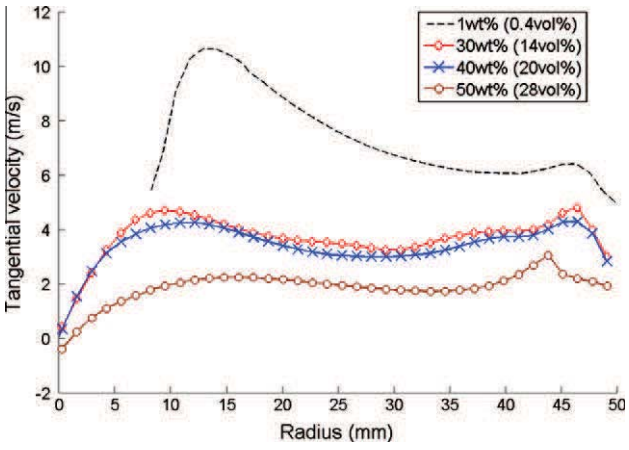

Fig. 10. Water tangential velocity profile in the cylindrical section of the hydrocyclone, taken 100 mm under the roof.

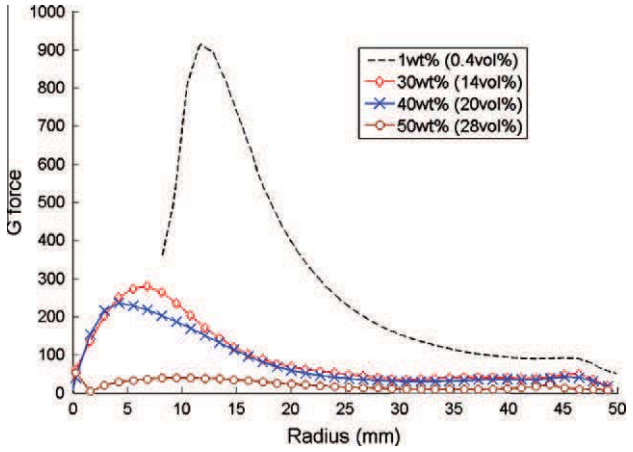

Fig. 11. G-force profiles in the cylindrical section of the hydrocyclone, taken 100 mm under the roof.

Fig. 12 shows the distribution of liquid volume fraction (alt. the distribution of solids concentration) inside the hydrocyclone. With 30 wt% and 40 wt% feed solids content, it is apparent that particles undergo a separation inside the hydrocyclone, with a strong gradient of water (alt. solids) concentration from bottom to top of the hydrocyclone. In the 50 wt% case, water (alt. solids) concentration is homogeneously distributed throughout the body of the hydrocyclone, which implies that little separation is taking place inside the hydrocyclone. Due to the solid concentration, local viscosity of the suspension increases, which dissipates the energy that would otherwise be available to operate the separation inside the hydrocyclone.

According to Figs. 13 and 14, the tangential velocity and the associated G-force decrease steadily from the top to the bottom of the hydrocyclone. The bottom of the conical section is filled with particles and no longer contributes to the classification perfor-

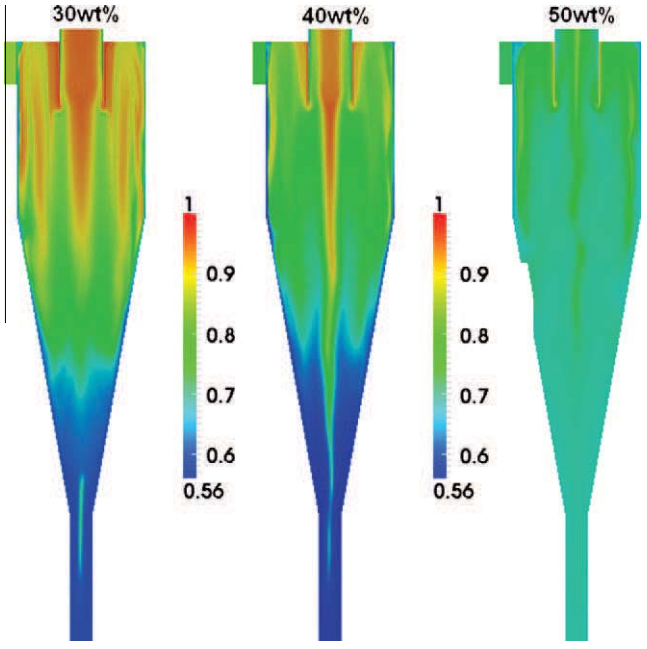

Fig. 12. Distribution of liquid volume fraction (=1 – solid volume fraction) inside the hydrocyclone.

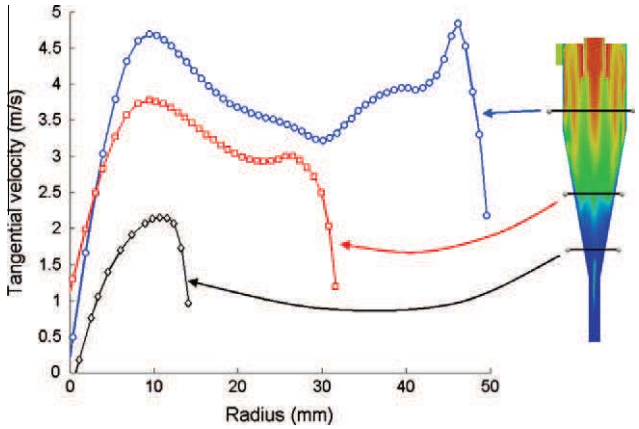

Fig. 13. Evolution of the tangential velocity along the height of the hydrocyclone with 30 wt% feed solids content.

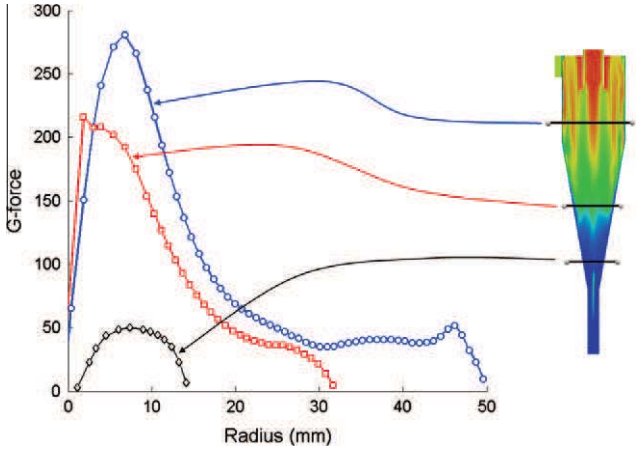

Fig. 14. Evolution of the G-force profiles along the height of the hydrocyclone with 30 wt% feed solids content.

mance of the hydrocyclone. The solid that fills this region of the hydrocyclone reduces the volume available for separation, as it gives an effective geometry for classification that is different from the physical geometry of the hydrocyclone. In the end, the simulation results show that the internal geometry of the hydrocyclone where swirling flow is occurring gradually evolves from that of a classifying cyclone to that of a stub cyclone. The notion of effective versus physical geometry of the hydrocyclone, as modified by the solids concentration inside the hydrocyclone, is deemed an important concept that underlies separation efficiency of the hydrocyclone.

4.2. Spigot diameter influence

As discussed in the previous Section 4.1, an increase of the total solids mass inside the hydrocyclone reduces the separation performance by slowing down the tangential velocity (hence the G-force) inside the hydrocyclone, which is the real separation driver. This also yields an increase in both water and fines recovery to the underflow. A further decrease of the spigot diameter from 18 mm to 6 mm was found in Section 3.2.2 to give a lower recovery to underflow with both fines and water under the same feed conditions, recalling that the hydrocyclone was already roping with the 18 mm spigot.

The same trend is found by numerical simulations, however simulation tends to overestimate the effect of spigot diameter on

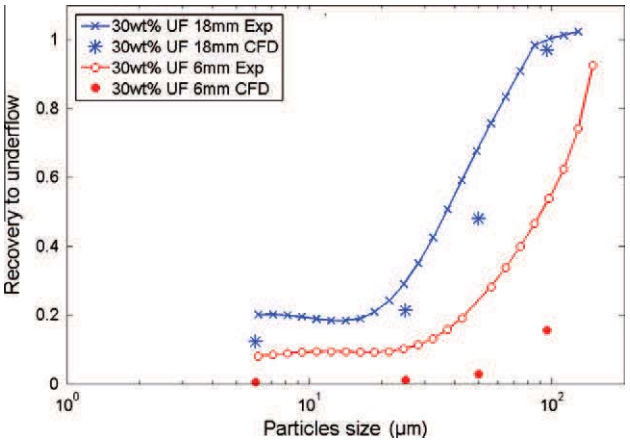

Fig. 15. Influence of spigot diameter on separation curves.

Table 4
Influence of spigot diameter on the mass of liquid and solids inside the hydrocyclone body.

	Water (kg)	Silica (kg)					
		6 μm	25 μm	50 μm	96 μm	Total	
UF 6 mm	1.339	0.146	0.172	0.276	0.391	0.985	42 wt%
UF 18 mm	1.509	0.163	0.182	0.247	0.241	0.832	36 wt%
Variation	11%	10%	5%	−12%	−62%	−18%	

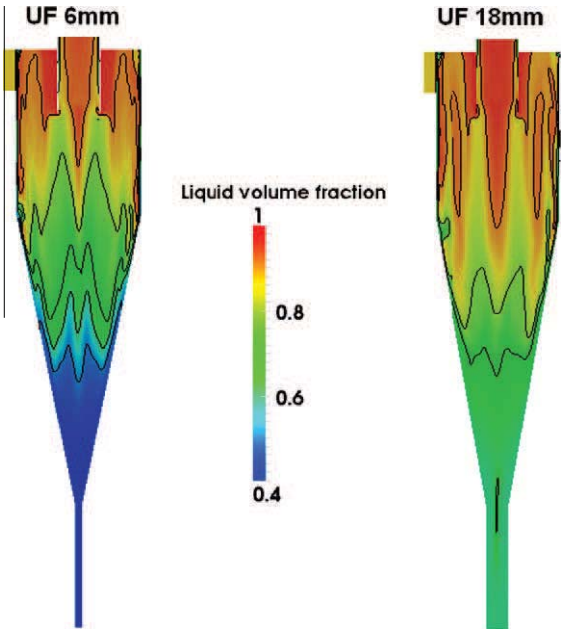

Fig. 16. Influence of spigot diameter on liquid volume fraction.

separation performance (see Fig. 15). As per the measurement, the fines ratio decreases with decreasing spigot diameter, which is correlated to the water split.

The change from the 18 mm to the 6 mm spigot affects particles in a different manner, which depends on their diameter. This can be appreciated through the evolution of the mass of individual size classes inside the hydrocyclone are reported in Table 4.

With a small spigot diameter, the largest particles are more concentrated inside the hydrocyclone, and more of the smaller

particles report to the overflow. Despite the reduced separation performance (see Fig. 15), the hydrocyclone is able to separate particles under the conditions of the test.

Fig. 16 reveals that there is a low solids concentration area in the cylindrical part of the hydrocyclone with both spigots. The consequence is that there is still sufficient tangential velocity (see Fig. 17) to yield some classification. The increase in cut size is not correlated with a decrease in tangential velocity 100 mm from the roof, as seen with the larger spigot at the highest solids concentration (Fig. 10).

The change in spigot diameter is responsible for this evolution of the behavior. According to Table 4 and Fig. 18, there is almost twice as much of the largest particles inside the hydrocyclone with the 6 mm diameter spigot than with the 18 mm spigot. Moreover, due to the small underflow diameter and by the compaction of particles in the conical part, the flow rate passing through the vortex finder increases and drives out more particles, irrespective of their diameter. With the 6 mm diameter spigot, 99% of the feed mass flow rate report to the overflow, which would correspond to the hydrocyclone choking in practice. Despite the fact that the simulations give interesting trends about the effect of dense regime on hydrocyclone separation behavior, it also shows that the current simulation CFD code is not yet able to predict all that happens inside the hydrocyclone as the hydrocyclone did not choke under these conditions. The discrepancies can also been seen in the predicted and measured partition functions of Fig. 15.

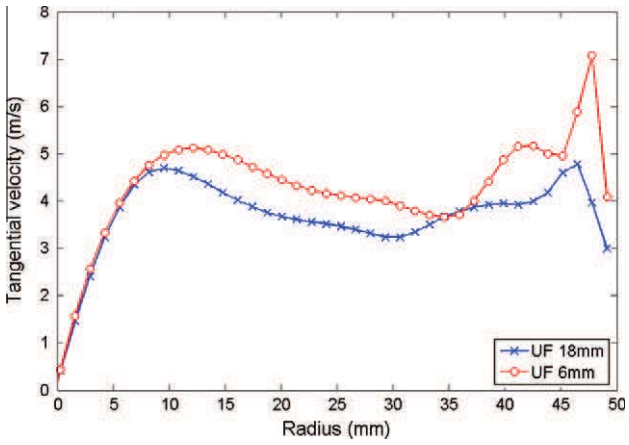

Fig. 17. Water tangential velocity profile in the cylindrical section of the hydrocyclone, taken 100 mm under the roof.

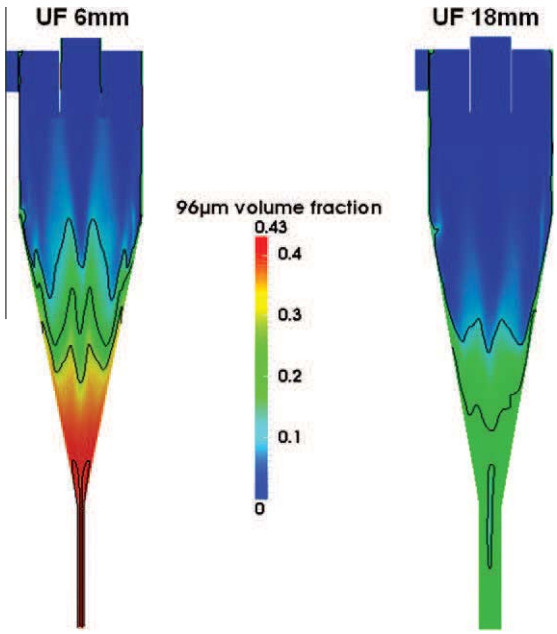

Fig. 18. Influence of spigot diameter on 96 µm diameter particles.

5. Conclusion and perspectives

CFD simulation offers significant potential for studying and understanding the separation mechanisms that take place inside a hydrocyclone. This can potentially give practitioners and researchers interesting guidelines for improving the performance of hydrocyclones and possibly improve their design.

There are many circumstances where hydrocyclone performance and dense flow are intertwined, however the effect of dense regimes inside a hydrocyclone are not understood. This work has established that CFD modeling can easily provide meaningful information about the properties of the swirling flow inside a hydrocyclone where experimental investigations would be utterly complex.

Comparison between CFD simulation results and measured values of solids split and separation functions measured on a 100 mm diameter hydrocyclone permitted conclusion that CFD simulations are able to predict performance trends, even under extreme roping conditions.

Through varying feed solids concentration and spigot diameters, a number of distinct operating regimes were produced inside the hydrocyclone. It was found that solids concentration is more or less evenly distributed throughout the hydrocyclone. Dense regions can form inside the hydrocyclone, mainly towards the bottom part of the conical section, which dissipate energy through viscous effects. The swirling flow, with the high tangential velocities (G-force) that are the classification driver cannot develop throughout the entire hydrocyclone body. This can be described as the hydrocyclone having an apparent, or effective geometry that differs from the physical one. At the highest solids concentration tested in this study, the conical section of the hydrocyclone was almost entirely filled with a packed bed of particles, so that the apparent geometry resembled that of a stub cyclone, yielding a thickening behavior of the hydrocyclone with nearly all the process water reporting to the overflow.

Overall, this study has established that it is possible to simulate the behavior of the swirling flow inside hydrocyclone under dense regimes. Even though it is necessary to continuously improve on the quality of the physics embedded into the CFD model, it was found that analysis of simulation results can help understand the separation trends observed in experiments. A great deal of information that is directly relevant to practical operation of hydrocyclones can be made from analysis of the flow characteristics inside the hydrocyclone. It is believed that many important practical issues such as short-circuiting, the Rf factor or the fish-hook effect will soon find interesting explanations from analysis of CFD simulations.

Acknowledgements

The authors would like to acknowledge TOTAL S.A. for funding this study through a PhD CIFRE program and the scientific support of C. Leroi and C. Yacono. The simulations were performed at the High Performance Computing centre CALMIP (Calcul en Midi-Pyrénées) under the project P0406.

References

Batrak, O., Patino, G., Simonin, O., Flour, I., Le Guevel, T., Perez, E., 2005. Unlike particles size collision model in 3d unsteady polydispersed simulation of circulating fluidised bed. In: 8th International Conference on Circulating Fluidized Bed, Hangzhou, China.

Brennan, M., 2006. CFD simulations of hydrocyclones with an air core comparison between large eddy simulations and a second moment closure. Chemical Engineering Research and Design 84, 495–505.

Chang, Y., Ilea, C., Aasen, Ø., Hoffmann, A., 2011. Particle flow in a hydrocyclone investigated by positron emission particle tracking. Chemical Engineering Science.

Davailles, A., Climent, E., Bourgeois, F., 2012. Fundamental understanding of swirling flow pattern in hydrocyclones. Separation and Purification Technology. doi:10.1016/j.seppur.2011.12.011.

Delgadillo, J., Rajamani, R., 2005. A comparative study of three turbulence-closure models for the hydrocyclone problem. International journal of mineral processing 77, 217–230.

Ergun, S., 1952. Fluid flow through packed columns. Chemical Engineering Progress 48, 89–94.

Galassi, M., Coste, P., Morel, C., Moretti, F., 2009. Two-phase flow simulations for PTS investigation by means of NEPTUNE CFD code. Science and Technology of Nuclear Installations 2009, 12.

Galvin, K., Smitham, J., 1994. Use of X-rays to determine the distribution of particles in an operating cyclone. Minerals Engineering 7, 1269–1280.

Gobin, A., Neau, H., Simonin, O., Llinas, J., Reiling, V., Sélo, J., 2003. Fluid dynamic numerical simulation of a gas phase polymerization reactor. International Journal for Numerical Methods in Fluids 43, 1199–1220.

Gourdel, C., Simonin, O., Brunier, E., 1999. Two-maxwellian equilibrium distribution function for the modelling of a binary mixture of particles. Circulating Fluidized Bed Technology, vol. VI. Frankfurt am Main, Germany.

Hsieh, K., 1988. Phenomenological Model of the Hydrocyclone. Ph.D. Thesis. Dept. of Metallurgical Engineering, University of Utah.

Hsieh, K., Rajamani, R., 1991. Mathematical model of the hydrocyclone based on physics of fluid flow. AIChE Journal 37.

Kelsall, D., 1952. A study of the motion of solid particles in a hydraulic cyclone. Chemical Engineering Research and Design 30, 87–108.

Launder, B., Reece, G., Rodi, W., 1975. Progress in the development of a reynolds-stress turbulence closure. Journal of fluid mechanics 68, 537–566.

Laviéville, J., Boucker, M., Quemerais, M., Mimouni, S., Mechitoua, N., 2006. NEPTUNE_CFD V1.0 – Theory Manual. NEPTUNE Report H-I81-2006-04377-EN – Nept_2004_L1.2/3, EDF R& D.

Laviéville, J., Simonin, O., 1999. Equations et modèles diphasiques du Code Astrid 3.4 et du Code saturne polyphasique. Technical Report HE-44/99/041/A, EDF R& D.

Nageswararao, K., Wiseman, D., Napier-Munn, T., 2004. Two empirical hydrocyclone models revisited. Minerals Engineering 17, 671–687.

Neesse, T., Dueck, J., 2007. Air core formation in the hydrocyclone. Minerals Engineering 20, 349–354.

Neesse, T., Schneider, M., Golyk, V., Tiefel, H., 2004a. Measuring the operating state of the hydrocyclone. Minerals Engineering 17, 697–703.

Neesse, T., Schneider, M., Golyk, V., Tiefel, H., Dueck, J., Buntenbach, S., 2004b. Hydrocyclone operation at the transition point rope/spray discharge. Minerals Engineering 17, 733–737.

Ozel, A., Fede, P., Simonin, O., 2010. 3D numerical prediction of gas-solid flow behavior in CFB risers for Geldart A and B particles. In: Proceedings of the 20th International Conference on Fluidized Bed Combustion.

Simonin, O., 1996. Continuum Modelling of Dispersed Two-phase Flows Combustion and Turbulence in Two-phase Flows (Lecture Series 1996–02). Von Karman Institute for Fluid Dynamics, Rhode Saint Genese.

Slack, M., Prasad, R., Bakker, A., Boysan, F., 2000. Advances in cyclone modelling using unstructured grids. Transactions of IChemE 78, 1098–1104.

Srivastava, A., Sundaresan, S., 2003. Analysis of a frictional-kinetic model for gas-particle flow. Powder Technology 129, 72–85.

Wen, C., Yu, Y., 1965. Mechanics of Fluidization. In: Chem. Eng. Prog. Symp. Ser., p. 100.